Article:

Murray, T., Nettles, M., Selmes, N. et al. (9 more authors) (2015) Reverse glacier motion during iceberg calving and the cause of glacial earthquakes. Science, 349 (6245). pp. 305-308. ISSN 0036-8075

https://doi.org/10.1126/science.aab0460

Science AAAS

Supplementary Materials for

Reverse Glacier Motion During Iceberg Calving and the Cause of Glacial Earthquakes

T. Murray, M. Nettles, N. Selmes, L. M. Cathles, J. C. Burton, T. D. James, S. Edwards, I. Martin, T. O'Farrell, R. Aspey, I. Rutt, and T. Baugé
.

correspondence to: t.murray@swansea.ac.uk

This PDF file includes:

Materials and Methods

Glacial earthquake analysis

We detected glacial earthquakes by back-propagation of vertical-component seismic signals recorded at stations of the global seismographic network (*13, 23*). We also inspected back-propagated seismograms and array stacks interactively to identify earthquakes too small for automatic detection by our standard algorithm (*10*). The earthquakes were initially identified independently of image analysis; one additional weak seismic signal was confirmed as an earthquake after comparison with camera imagery.

We modelled the seismic waveforms using a centroid-single-force (CSF) formalism (*11, 25*) to confirm earthquake locations and obtain earthquake source parameters including the orientation of the force active during the earthquake, the earthquake CSF amplitude, and the earthquake centroid time, t_c (centroid of the temporal force history). The inversion approach and data processing follow ref. 6. We assume a force-time history 50 s long in which the force has a constant amplitude for one half the earthquake duration, followed by a constant amplitude of opposite polarity for the remainder of the duration; that is, the time function is a square wave of one cycle. The centroid time corresponds to the time of the polarity reversal of the force at the earthquake half duration. We note that the force-time history used in the seismic inversions is not derived from the seismic data, but is prescribed. The most important feature of the time function for the current analysis is the rapid change in force amplitude that occurs at t_c. As discussed in ref. 16, the true earthquake time function may not be symmetric, and may have longer duration. Here, we choose to use the 50-s boxcar function for consistency with previous systematic studies of glacial earthquakes (*6, 10, 11, 13, 16*).

We performed an experiment using the scaled force and pressure timeseries from the laboratory experiments to provide input, time-varying force histories simulating a glacial earthquake. The pressure timeseries were converted to a vertical force history by multiplication by the map-view area of the iceberg calved, as determined from photogrammetric analysis. Vertical and horizontal force histories were downsampled to one sample every 10 s and modelled as a series of overlapping isosceles triangles of varying height. Synthetic seismograms were calculated by summation of normal modes in the preliminary reference Earth model (PREM) (*26*) for each triangular sub-source and the seismograms summed to form the complete records. Seismograms were calculated for stations at a range of distances and azimuths representative of those typically available for analysis of glacial earthquakes at Helheim Glacier. The seismograms were then inverted using the same approach as for data seismograms to obtain earthquake parameters.

Photogrammetric analysis

Two 15.1 megapixel Canon 50D single lens reflex (dSLR) cameras were installed in stereo configuration on the bedrock margins of Helheim Fjord ~4 km down-fjord (east) from and looking at the calving front. The cameras were manually synchronized to take hourly photographs and operated between 2013 DOY 196 and 245. Fixed 28 mm wide-angle lenses were used in order to capture the majority of the calving front. Digital elevation models (DEMs) were produced photogrammetrically from stereo imagery using the 3D visualization capabilities of SocetSET digital photogrammetry suite alongside the bundle adjustment and DEM extraction components of Topcon's ImageMaster. Ground control information was extracted from a 2013 lidar DEM (*27*). We compared DEMs prior to and following calving events to obtain three-dimensional calving geometry, including the locations of the calving margins. Detailed methodology of the photogrammetric processing is described in the Methods and Supplementary Material of ref. 8.

Estimates of glacier thickness and iceberg aspect ratio

Estimates of glacier thickness for the DOY 206 and 212 events were made using IceBridge MCoRDS L3 Gridded Ice Thickness, Surface, and Bottom, Version 2 (*28*). Mean bottom elevations of flightline points that fell within the areal extent of each calving event provided our estimates. In the vicinity of the heavily crevassed calving front, errors are estimated to be ±60 m (*8*).

Iceberg aspect ratios, defined as the along-flow width of the calved iceberg to the estimated iceberg height, were estimated using the photogrammetric results and an equivalent rectangular iceberg, together with the estimated glacier thickness. Idealized rectangular dimensions were constructed by measuring iceberg cross-glacier and along-flow widths and adjusting these to rectangular dimensions matching the measured map-view area of ice lost in each calving event.

GPS data processing

GPS sensors on ice and bedrock used Ashtech MB100 dual-frequency geodetic receiver boards and ASH111661 dual-frequency antennas.

The position of the base station located on bedrock was estimated using the Precise Point Positioning (PPP) method (*29*) with GIPSY-OASIS version 6.2 software from JPL. In addition to base-station coordinates and a receiver clock offset, a zenith wet tropospheric delay and tropospheric gradients were estimated. JPL fiducial orbit and 30-s clock products were held fixed. Hydrostatic zenith delay was modelled (*30*) with zenith delays mapped to elevation using the Global Mapping Function (GMF) (*31*). Ocean tide loading displacements were corrected for using the FES2004 model (*32*) and solid Earth tides were corrected according to the IERS 2010 conventions (*33*). Carrier-phase ambiguities were fixed to integers where possible (*34*).

GPS data from sensors on the glacier surface were processed using the relative carrier-phase method with TRACK version 1.29 software (*35*) from GAMIT 10.50. Kinematic positions were estimated with respect to the fixed base station using the ionosphere-free linear combination of L1 and L2 observations (LC). Baseline lengths ranged from 1.5-5.6 km. An elevation-angle cutoff of 10° was applied. We used orbit and high-rate (5 s) clock products from CODE (*36*). Zenith delays were modelled and mapped as above (*30, 31*) but no wet tropospheric correction was estimated. Observations were processed on a day-of-year basis, with prior-day and following-day orbit and clock data appended to facilitate TRACK's interpolation scheme. Kinematic site motion was modelled using a random-walk stochastic model. The model standard deviation was set at 0.01 $m/s^{0.5}$. Position time series were filtered to exclude data where the number of unfixed biases was greater than 2, the number of double differences was fewer than 10, or the height uncertainty was greater than 0.1 m.

Laboratory Experiments

Data acquisition

The laboratory experiments were performed in a fresh-water tank 244 cm long, 30 cm wide, and 30 cm tall, similar to tanks used previously (*19, 24, 37*). A model glacier terminus was secured at one end of the tank. Plastic icebergs made from polyethylene with a density nearly identical to glacier ice (920 kg/m^3) and height H_L = 20.3 cm, width εH_L , and cross-tank dimension D_L = 26.7 cm were placed flush against the terminus and allowed to capsize spontaneously under the influence of gravitational and buoyancy forces. Experiments were conducted with icebergs of aspect ratio ε = 0.22, 0.28, 0.43, 0.54. Three levels of perforated plastic sheet were secured at an incline to the water's surface at the other end of the tank to damp seiche modes (*38*). Two different model termini were used: one with an embedded pressure sensor that monitored pressure at three water depths and one that was coupled to four force sensors located at each corner of the terminus. The pressure and force data were acquired at a rate of 200 Hz.

The pressure sensor (GEMS™) had a maximum range of 2500 Pa hydrostatic pressure and a response time of 5 ms. We used the pressure data recorded at the deepest of the three measured depths in our analyses. The force sensors (Strain Measurement Devices) each had a maximum range of 0.5 N. The sensors rely on mechanical deflection to measure the force. The terminus used to measure the force was designed so that its frequency response was flat in the bandwidth produced by the motion of the iceberg and subsequent waves. The total force was calculated by summing the signals from all four sensors and inherently represents a sum of contact and pressure forces acting on the terminus. Repeat experiments showed nearly identical results for both the pressure and force measurements. The results shown in Figure 3 represent the average of 3 force measurements and 5 pressure measurements. The position and orientation of the plastic iceberg were determined by image analysis and were used to synchronize the force and pressure measurements in time.

Scaling of laboratory data

In order to compare lab data to field data, the forces and pressures measured in the laboratory were scaled up to match the dimensions of icebergs at Helheim Glacier, as measured by photogrammetry. Following previous studies (*19, 24*), the laboratory data were scaled by powers of the ratio of the iceberg height in the field, H_F, to the iceberg height in the laboratory, H_L. Because the gravitational potential energy released by iceberg capsize scales as H^4 (*24, 39*), force measurements from the laboratory were scaled by $(H_F/H_L)^3$, pressure measurements by (H_F/H_L) and time scales by $(H_F/H_L)^{1/2}$. This method of scaling implicitly assumes that the flow of the water in the lab and in the field can be considered dynamically similar. The Reynolds number for flow is ~10^{10} in the field and ~10^5 in the lab, but the flow is turbulent in both cases and typical drag coefficients on solid bodies vary little in this flow regime (*19, 24*).

Prediction of glacier deflection

The scaled force and pressure are used to predict the time history of deflection of the glacier-terminus region. We modeled the deflection of the calving region as an elastic response to the force applied. The total force per unit area acting on the glacier terminus produces a linear deflection orthogonal to the calving front such that $F_{tot}/A_F = E\Delta L/L$, where E is the Young's modulus of glacial ice (~1 GPa; refs. *40, 41*). The area over which the total force acts is the surface area of the terminus adjacent to the capsizing iceberg, $A_F \sim H_F D_F$, where D_F is the cross-glacier length of the calved iceberg. In Figure 3, the value of L was chosen so as to best match the GPS data (L=4.9 km). The length-scale L likely represents the approximate distance from the terminus to the grounding zone.

The pressure reduction in the water behind the rotating iceberg creates a downward force on the front of the glacier (in contrast to the upward force it causes on the solid earth). The water under the ungrounded region of the glacier responds to this reduction in pressure (~ 5 x 10^4 Pa), creating a net vertical force acting on the glacier over an area $A_P \sim \kappa L D_F$, where κ is the fraction of the length L over which the pressure is initially reduced beneath the glacier. We model the glacier tongue as an Euler–Bernoulli beam of length L with a varying load due to gravitational, buoyant, and pressure forces acting on it. Our simplified model assumes the beam is clamped at the grounding line and stress free at the terminus. Varying κ to match the L determined from the horizontal deflection (L = 4.9 km) yields κ = 0.02, such that the pressure load is applied over a narrow region parallel to the glacier terminus consistent with the dimensions of the capsizing iceberg.

For the comparison of predicted and observed deflection shown in Figure 3, we low-pass filter the scaled pressure and force traces using a 5-pole Butterworth filter with a corner period of 40 s. The pressure and force records are dominated by the very-long-period deflection signal, and this choice of filtering does not affect our results or interpretation, but serves to reduce the presence of high-frequency oscillations of the water column in the tank that are expected to be damped by ice mélange in the glacier fjord. It also removes low-amplitude, very-high-frequency sensor noise.

We find that the model iceberg aspect ratio for which the scaled laboratory data best match the observed GPS data shown in Figure 2 is ε = 0.22, compared to a measured iceberg aspect ratio from field data of 0.23.

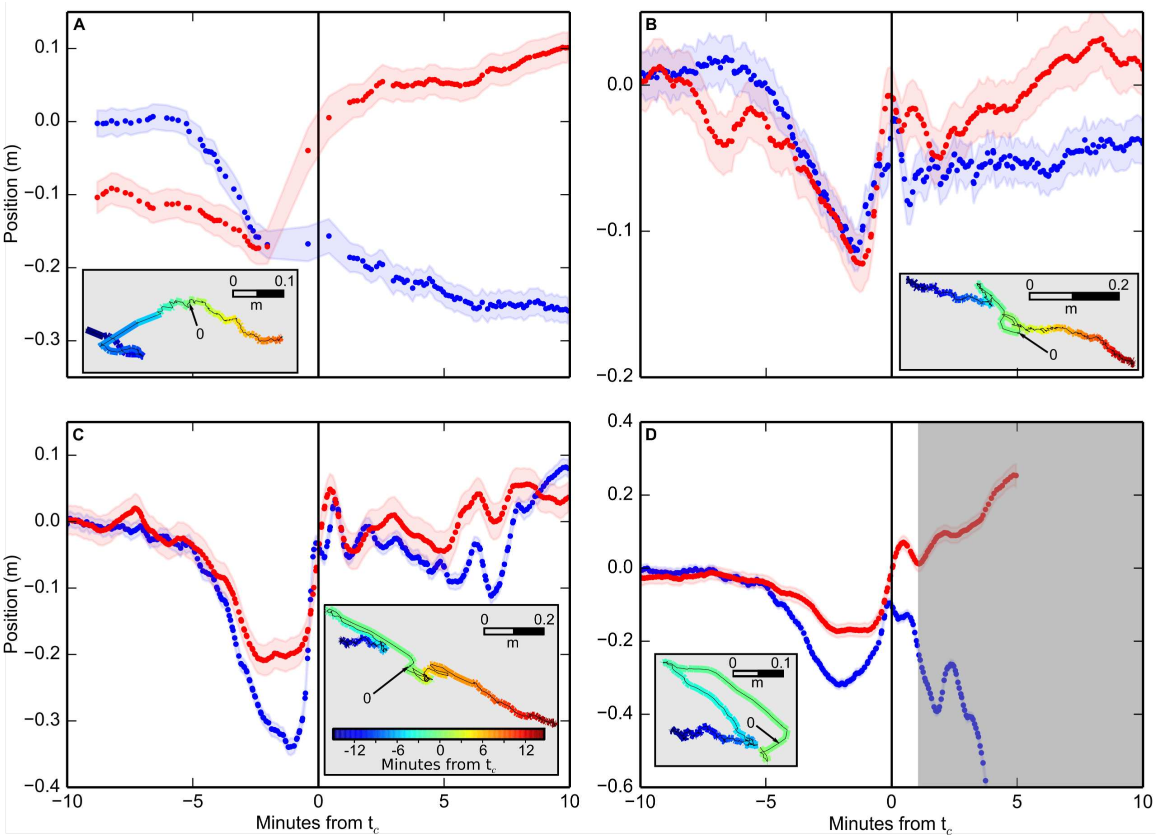

Fig. S1.

Additional examples of glacier response at times of glacial earthquakes. (A) Sensor 6 at 03:13 on DOY 206 2013; some data missing due to communications failure. (B) Sensor 15 at 03:13 on DOY 206 2013. (C) Sensor 1 at 12:56 on DOY 206 2013. (D) Sensor 15 at 12:56 on DOY 206 2013; sensor is lost shortly after this event. Symbols as in Figure 2. Horizontal displacement for B-D has trend of 30-10 mins before t_c removed (B=27.6 m/day, C=27.5 m/day, D=29.4 m/day) and for panel A the trend from 10-5 mins before t_c (36.0 m/day). Height has mean removed. Insets (grey boxes) show plan view of GPS trace during 30 minutes around t_c, marked as 0; in panel (D), grey shaded region (showing time of imminent sensor loss) in main panel is excluded from inset.